

RESEARCH ARTICLE

10.1029/2019JB019242

Key Points:

- Micropillar compression experiments were used to measure the yield strength of an olivine single crystal at room pressure and temperature
- Strain was accommodated by shear bands, which were found to amorphized by deformation
- Strained regions are enriched in Fe, suggesting that preexisting variations in cation concentration play a role in shear band nucleation

Supporting Information:

- Supporting Information S1

Correspondence to:

P. Skemer,
pskemer@wustl.edu

Citation:

Kranjc, K., Thind, A. S., Borisevich, A. Y., Mishra, R., Flores, K. M., & Skemer, P. (2020). Amorphization and plasticity of olivine during low-temperature micropillar deformation experiments. *Journal of Geophysical Research: Solid Earth*, 125, e2019JB019242. <https://doi.org/10.1029/2019JB019242>

Received 16 DEC 2019

Accepted 25 MAR 2020

Accepted article online 6 APR 2020

Amorphization and Plasticity of Olivine During Low-Temperature Micropillar Deformation Experiments

Kelly Kranjc¹, Arashdeep S. Thind¹ , Albina Y. Borisevich², Rohan Mishra^{1,3} , Katharine M. Flores^{1,3}, and Philip Skemer⁴ 

¹Institute of Materials Science and Engineering, Washington University in St. Louis, St. Louis, MO, USA, ²Center for Nanophase Materials Sciences, Oak Ridge National Laboratory, Oak Ridge, TN, USA, ³Department of Mechanical Engineering and Materials Science, Washington University in St. Louis, St. Louis, MO, USA, ⁴Department of Earth and Planetary Sciences, Washington University in St. Louis, St. Louis, MO, USA

Abstract Experimentally quantifying the viscoplastic rheology of olivine at the high stresses and low temperatures of the shallow lithosphere is challenging due to olivine's propensity to deform by brittle mechanisms at these conditions. In this study, we use microscale uniaxial compression tests to investigate the rheology of an olivine single crystal at room pressure and temperature. Pillars with nominal diameters of 1.25 μm were prepared using a focused ion beam milling technique and were subjected to sustained axial stresses of several gigapascal. The majority of the pillars failed after dwell times ranging from several seconds to a few hours. However, several pillars exhibited clear evidence of plastic deformation without failure after 4–8 hr under load. The corresponding creep strain rates are estimated to be on the order of 10^{-6} to 10^{-7} s^{-1} . The uniaxial stresses required to achieve this deformation (4.1–4.4 GPa) are in excellent agreement with complementary data obtained using nanoindentation techniques. Scanning transmission electron microscopy observations indicate that deformation occurred along amorphous shear bands within the deformed pillars. Electron energy loss spectroscopy measurements revealed that the bands are enriched in Fe and depleted in Mg. We propose that inhomogeneities in the cation distribution in olivine concentrate stress and promote the amorphization of the Fe-rich regions. The time dependence of catastrophic failure events suggests that the amorphous bands must grow to some critical length scale to generate an unstable defect, such as a shear crack.

1. Introduction

Olivine is the most volumetrically abundant mineral in Earth's upper mantle, and its viscoplastic rheology exerts first-order control on mantle convection and the motion of tectonic plates (Hirth & Kohlstedt, 2003; Karato & Wu, 1993). Microstructural observations of naturally deformed mantle rocks indicate that that deformation takes place mainly by dislocation or diffusional creep (e.g., Jaroslow et al., 1996; Nicolas et al., 1971). Quantitative flow laws for olivine at these conditions are constrained by extensive laboratory experimentation, which have shown that deformation may be accommodated by a combination of diffusional creep (Mei & Kohlstedt, 2000a), dislocation creep or glide (Mei & Kohlstedt, 2000b), and dislocation-accommodated grain boundary sliding (Hansen et al., 2011). However, at low temperatures and pressures, and typical laboratory strain rates, olivine deforms via brittle fracture rather than ductile flow. This propensity to fail by brittle processes inhibits direct investigations of rheology at conditions relevant to the strong, shallow lithosphere near the brittle-plastic transition (Druiventak et al., 2011). Due to the challenge of conducting experiments on olivine rheology at low pressures and temperatures, the most detailed flow laws for low-temperature plasticity are parameterized through extrapolation from higher pressures and temperatures (Mei et al., 2010; Raterron et al., 2004). This extrapolation imposes a degree of uncertainty (Hirth & Kohlstedt, 2015; Jain et al., 2017) that affects modeling and other geophysical interpretations of lithospheric dynamics (Freed et al., 2006). The aim of this work is to constrain further the mechanical properties of olivine at low temperatures.

Recently, we have also investigated the low-temperature rheology of olivine using nanoindentation (Kranjc et al., 2016). While the elastically deforming material surrounding the indent effectively prevents brittle

failure and enables the study of plastic flow, the complex, multiaxial stress state induced by indentation complicates comparisons with traditional uniaxial measurements of yield behavior. In this work, we apply a focused ion beam (FIB) micromachining technique to produce microscale specimens with a simple cylindrical geometry that can be loaded in uniaxial compression. Micropillar compression has been used extensively to induce plastic deformation in materials that exhibit macroscale brittle failure; a size-dependent transition from brittle behavior for large specimens to plastic deformation in small specimens has been observed in diamond (Banerjee et al., 2018), silicon (Korte & Clegg, 2011), MgAl_2O_4 spinel (Korte & Clegg, 2009), and metallic glass (Jang & Greer, 2010; Volkert et al., 2008). The exact mechanism(s) behind this phenomenon are still unclear; however, several explanations have been proposed, including the presence of fewer flaws in smaller samples (Gao et al., 2003), an increase in fracture energy (Östlund et al., 2009), or a decrease in crack driving force (Östlund et al., 2011).

While the microscale geometry does not completely mitigate brittle failure in olivine, we show here that room temperature plastic deformation is achieved in several specimens. Ex situ analysis of plastically deformed specimens using scanning transmission electron microscopy (STEM) reveals that the deformation is not associated with dislocation motion but rather with the formation of a new type of planar defect. These defects are characterized by bands of amorphous material, tens of nanometers thick, across which macroscopic shear and rotations in crystallographic orientation are observed. The amorphous shear bands are locally enriched in Fe relative to Mg, and Fe exhibits a change in oxidation state from +2 to +3. Similar mis-oriented and amorphous regions were not observed in undeformed materials. We infer that deformation induced amorphization is the mechanism by which plastic strain is accommodated. Although deformation was not dislocation mediated, as is commonly observed in previous experiments and in the rock record, the flow stress measured in these room temperature experiments is in excellent agreement with the low-temperature plasticity flow law determined from the earlier nanoindentation study (Kranjc et al., 2016). While the underlying deformation mechanisms are different, we suggest that micropillar compression testing and nanoindentation are, collectively, establishing an upper limit on the yield strength of olivine.

2. Experimental Procedure

2.1. Materials and Testing

A gem-quality single crystal of olivine was selected for micropillar deformation tests. Its composition was determined by electron probe microanalysis using a JEOL JXA-8200 to be relatively magnesium rich, with an $\text{Mg}\# = 93.3$. The specimen was oriented using electron backscatter diffraction, sectioned, and polished to produce a surface with normal $[110]_c$. (Following the convention used in Durham and Goetze (1977) and Bai and Kohlstedt (1992), “[110]_c” describes an orientation 45° from the [100] and [010] crystallographic directions and 90° to the [001] axis. That is, the subscript “c” denotes an imaginary cubic lattice aligned with the axes of the orthorhombic olivine lattice.) This orientation was selected to favor slip on the [100](010) slip system (Durham & Goetze, 1977). The specimen was then fixed to a stainless steel disc with H20E EPO-TEK silver conductive epoxy. The surface was coated with an 8-nm thick layer of iridium to prevent charging under the ion beam during FIB processing.

Cylindrical micropillars oriented with the $[110]_c$ direction parallel to the cylinder axis were fabricated using a Zeiss Crossbeam 540 FIB-scanning electron microscopy (SEM). This fabrication method uses Ga^+ ions to sputter the surface of the specimen in a desired geometric pattern. An annular milling technique commonly used for micropillar fabrication was employed here (Hütsch & Lilleodden, 2014). Using this approach, the Ga^+ beam grazes the side faces of the pillar, minimizing ion implantation and associated damage to the region of interest. In the present work, the annular milling was performed in four steps with sequentially smaller diameters. The beam current decreased from 15 nA in the first stage to 0.05 nA in the final step. The final ion dose was $5 \text{ nC}/\mu\text{m}^2$. The nominal final diameter of the pillars was $1.25 \mu\text{m}$, and the length of the pillars was approximately two times the diameter. Sample dimensions were measured in the SEM and are accurate to within $\sim 50 \text{ nm}$. The pillars sat at the center of an approximately $30\text{-}\mu\text{m}$ diameter well and remained attached to the bulk at one end, permitting easy handling. All specimens were inspected for surface flaws by SEM pretesting and posttesting.

Room temperature compression testing was performed using a Hysitron TI 950 nanoindenter equipped with a flat punch probe. Loads are applied with precision that is better than $0.1 \mu\text{N}$. The diameter of the probe is

20 μm , so there was complete contact between the top of the specimen and the face of the probe. Two monotonic load ramp tests were first performed on 1.1- μm diameter pillars at a loading rate of 50 $\mu\text{N/s}$ until failure occurred in order to establish an upper limit for subsequent creep testing (see Supporting Information Figure S1). Based on these results, tests were performed at constant loads of 5,000 μN for hold times of up to 4 hr. Pillars that survived 4 hr at this constant load were unloaded and examined in the SEM. Those that showed no evidence of deformation were then reloaded to 5,500 μN for up to four additional hours. During the hold segment of these tests, a 200-Hz sinusoidal load was superimposed over the set point load using the nano-dynamic mechanical analysis III module on the nanoindenter in order to continuously monitor the pillar stiffness. The amplitude of this sinusoidal load was selected so as to result in approximately 1 nm of dynamic displacement, corresponding to a microstrain of less than $\epsilon_\mu = 500$.

Pillars that appeared to have deformed during the sustained loading experiments, but did not fail catastrophically, were characterized using STEM. TEM foils of the longitudinal cross section of the pillars were prepared by FIB micromachining. To preserve the surface of the pillar and protect it from beam damage, a 2- μm thick layer of platinum was first deposited on the surface of the specimen, completely covering the pillar. An FEI Helios FIB was then used to remove a thin slice from approximately the center of the pillar. The foils were cut from the bulk pillar using a 21-nA beam current and were cleaned using a 2.5-nA current. Final thinning of the foils was performed at 0.79 nA. The resulting foils were mounted on Cu grids for investigation by STEM.

STEM imaging and electron energy loss spectroscopy (EELS) experiments were carried out using a Nion UltraSTEM™ 200 (operating at 200 kV) at Oak Ridge National Laboratory, which is equipped with a fifth-order aberration corrector and a cold field emission electron gun. EELS data sets were acquired using a Gatan Enfium spectrometer, with a collection semiangle of 33 mrad, an energy dispersion of 0.5 eV per channel, and pixel dwell time of 0.75 s. We performed principal component analysis, which is a multivariate statistical analysis method, to remove random-noise components from the EELS data sets. We used a power law to subtract the background signal from the characteristic core-loss edges for each element.

2.2. Data Analysis

Pillar dimensions were determined before and after compression testing from high-resolution SEM images. The taper of the pillars was found to be 2° to 3°. The axial stress was calculated by dividing the applied load by the cross-sectional area at the top of the pillar before testing because this is where the diameter is smallest and thus the stress is highest. The change in this cross-sectional area was not monitored during testing. The corresponding axial strain was calculated by dividing the measured axial displacement by the initial height of the pillar as measured from the SEM image before testing.

Due to thermal drift over the duration of the test, the displacement measurement from the instrument is not accurate for long durations at constant load. The 200-Hz load oscillation was applied during this segment to continuously monitor the storage stiffness (k') of the pillar:

$$k' = \frac{F_D \cos \varphi}{d_D} + m_T \omega^2 - k_T, \quad (1)$$

where F_D is the dynamic actuation force, φ is the phase shift between the dynamic force and dynamic displacement (d_D), m_T is the transducer mass, k_T is the transducer stiffness, and ω is the oscillation frequency. Using the storage stiffness determined at discrete intervals throughout the creep segment, the pillar displacement can be calculated by combining equations 2a and 2b below to obtain equation 2c:

$$k' \approx \frac{F_D}{d_D}, \quad (2a)$$

$$\epsilon_D = \frac{d_D}{l} = \frac{F_D}{EA}, \quad (2b)$$

$$d = h_0 - l = h_0 - \sqrt{\frac{VE}{k'}}, \quad (2c)$$

where ϵ_D is the dynamic strain due to the dynamic displacement and l is the instantaneous length of the

deformed pillar. The dynamic strain is related to the dynamic force via Hooke's law, where A is the average cross-sectional area of the deformed pillar and E is the elastic modulus. The displacement of the top of the pillar due to plastic deformation, d , is simply the difference between the initial height of the pillar, h_0 , and the deformed length. Finally, in simplifying equations 2a–2c, the pillar volume, V , is assumed to be equal to A times l . However, in applying equation 2c to calculate the displacement of the pillar, the pillar volume was assumed to remain constant throughout the test and was calculated as a conical frustum:

$$V = \pi \left[\frac{(h_0 \tan \beta + r_0)^3 - r_0^3}{3 \tan \beta} \right], \quad (3)$$

where β is the taper angle and r_0 is the radius of the top of the pillar.

When calculating the elastic modulus of pillar, both the pillar substrate and the taper of the pillar must be accounted for. When the pillar is compressed, there is some elastic deformation in the bulk material beneath the pillar, which results in an erroneously low modulus measurement. The Sneddon correction for elastic modulus, which was originally developed for nanoindentation, accounts for this (Sneddon, 1965). The formula to calculate the corrected modulus (E_S) is given in equation 4.

$$E_S = \frac{h_0}{\left(C_{\text{Tot}} - \frac{\sqrt{\pi(1-\nu^2)}}{E\sqrt{A_{\text{base}}}} \right) A_{\text{top}}}, \quad (4)$$

where E is the elastic modulus of the bulk polycrystalline mineral (200 GPa, after Evans & Goetze, 1979), ν is the Poisson's ratio of olivine (0.25, after Christensen, 1996), and A_{top} and A_{base} are the area of the top and base of the pillar, respectively. C_{Tot} is the total compliance due to sample displacement as well as displacement caused by the pillar indenting into the base material ($C_{\text{Tot}} = \frac{\partial d_{\text{Tot}}}{\partial P}$), where d_{Tot} is the measured displacement and P is the applied load. Because of imperfect alignment between the pillar and the flat punch, the loading portion of the stress-strain curve tends to have a slight nonlinearity. Thus, for specimens that remained intact at the end of the test, C_{Tot} was obtained from the unloading portion of the curve. The elastic modulus must further be corrected for taper because a larger degree of taper will artificially increase the calculated modulus (i.e., a tapered pillar will be stiffer than an ideal pillar) (Bharathula et al., 2010). Increasing the aspect ratio of the pillar (h_0/r_0) exacerbates this effect. The taper-corrected modulus was calculated as

$$E = \frac{E_{\text{apparent}}}{1 + \frac{h_0}{r_0} \tan \beta}. \quad (5)$$

Calculating the modulus using both equations 4 and 5 produces a result corrected for both base compliance and taper.

3. Results

3.1. Mechanical Data

Two 1.1- μm diameter pillars were loaded monotonically to failure to establish an upper limit for the applied stress during the sustained loading experiments. During monotonic loading, these pillars exhibited multiple unstable jumps in strain, most likely associated with individual brittle failure events. The stress at the first of these jumps was taken to be the brittle failure stress, which occurred at 3,800 μN (~ 4.0 GPa) and 5,600 μN (~ 5.9 GPa) in the two pillars, respectively.

The remaining pillars were deformed under sustained loading conditions at 5,000 or 5,500 μN (stresses of 4.1 or 4.5 GPa for a nominal 1.25- μm diameter pillar). Deformation fell into one of two categories: those that exhibited sudden jumps in strain, often after many seconds to hours at load; or those that formed one or more shear steps on the pillar surface in a stable fashion, without sudden jumps in strain, during the sustained hold. SEM images of pillars that strained rapidly are shown in Figure 1. These pillars exhibit a variety of deformation behaviors, such as axial splitting (Pillar 1), mushrooming (Pillars 2 and 3), and shearing (Pillars 4–6). The strain jump occurred at a wide range of times during testing (Table 1), from as little as

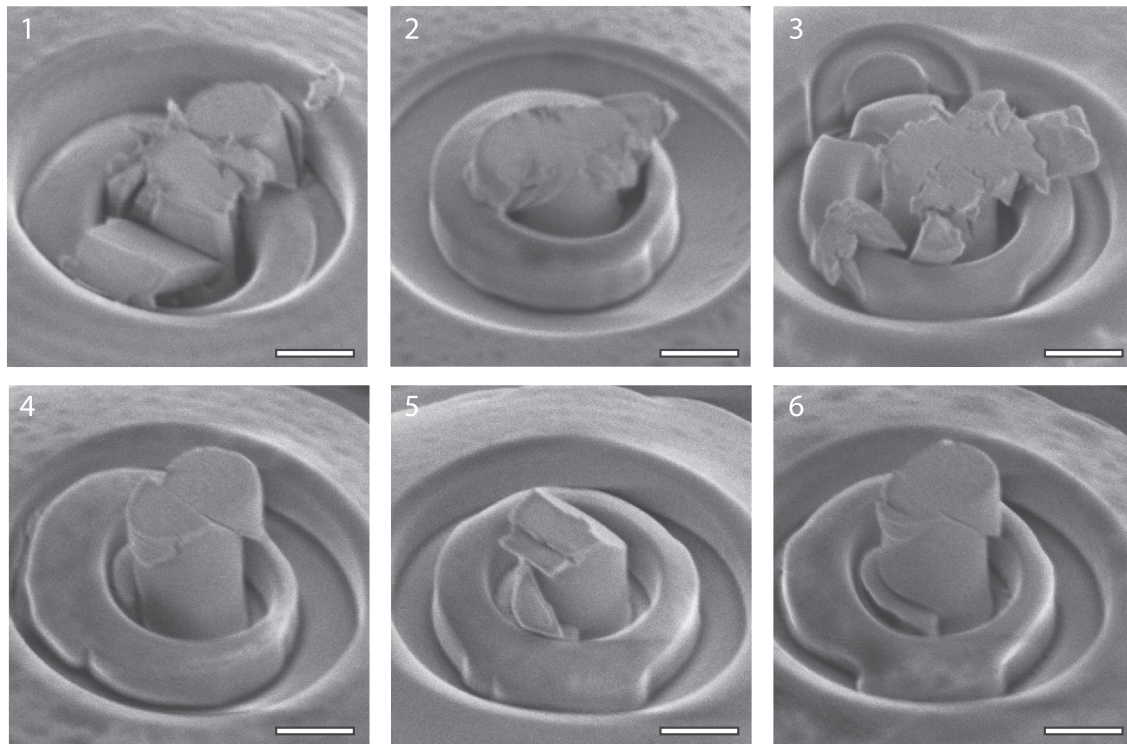


Figure 1. SEM images of pillars that failed catastrophically during room temperature testing at sustained loads. Modes of failure include shear fracturing and axial splitting. Pillars 4–6 had already undergone testing at 5,000 μN for 4 hr without obvious evidence of deformation and subsequently failed during a second test at 5,500 μN . Scale bar = 1 μm .

22 s after the 5,000- μN hold was established (Pillar 2), to as much as 3,567 s into the second hold at 5,500 μN (Pillar 6). Pillars that exhibited stable deformation during the sustained hold(s) are shown in Figure 2. White arrows in the figure identify the position of shear steps on the surface of the pillars, indicating plastic deformation had occurred during testing. The applied stresses and measured moduli for all pillars are summarized in Table 1.

Table 1

Mechanical Properties of the Pillars Shown in Figure 2, Including the Initial (Maximum) Applied Stress Calculated Using the Initial Pillar Diameter, the Final Applied Stress Calculated Using the Final Pillar Diameter, and the Elastic Modulus Measured Upon Unloading of the Pillar, Corrected for Base Compliance and Taper

Pillar #	σ_{max} (GPa)	Total duration before failure (s)	σ_f (GPa)	E_{corr} (GPa)	Strain rate (s^{-1})	IGSN
Catastrophic failure						
1	3.8	340				IESPM005Z
2	7.1	22				IESPM0061
3	4.0	1,230				IESPM0062
4	4.6	15,756				IESPM0063
5	4.3	16,203				IESPM0064
6	4.6	17,967				IESPM0065
Stable shear band formation						
7	4.4		3.8	160.3	4×10^{-6}	IESPM0066
8	4.1		4.0	167.7	1×10^{-6}	IESPM0067
9	4.1		4.0	199.0	-	IESPM0068
10	4.1		3.7	217.7	5×10^{-7}	IESPM0060

The axial strain (rates) of the pillars in Figure 2 were calculated using the displacement given by equation 2c (Pillar 9 was not measured due to instrument difficulties with the superimposed cyclic load during this experiment.) Pillar 7, which was the only pillar that survived both 4 hr at 5,000 μN and an additional 4 hr at 5,500 μN , exhibited the highest strain rate of $4 \times 10^{-6} \text{ s}^{-1}$ at the higher load (Table 1). Pillars 8 and 10 were tested for 4 hr at 5,000 μN , and their strain rates were calculated to be $1 \times 10^{-6} \text{ s}^{-1}$ and $5 \times 10^{-7} \text{ s}^{-1}$, respectively (see Figure S2).

3.2. STEM Analysis

To study the structural changes associated with deformation, TEM foils were prepared by FIB micromachining and examined using (S)TEM. The shear offsets observed in the SEM images (Figure 2) are associated with distinct shear bands that traverse the specimen at approximately 45° to the loading axis, as shown in the bright-field TEM image of Pillar 7 in Figure 3. To investigate the atomic-scale structure and composition of these shear bands, we performed aberration-corrected STEM imaging and EEL spectroscopy on selected pillars. A foil was prepared by FIB and rotated to a zone axis of [010] to facilitate high-resolution imaging. High-resolution images did not reveal any dislocation activity within

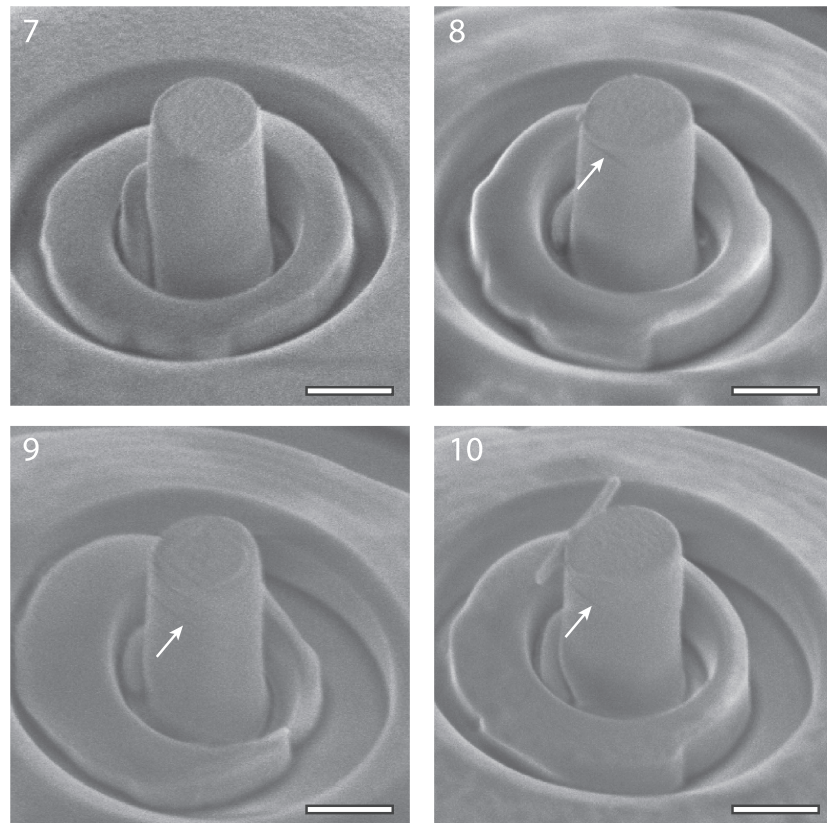


Figure 2. SEM images of pillars that exhibit shortening and/or crenulations on the outer surface (indicated by the white arrows), which are interpreted to be formed by shear bands. Pillar 7 was loaded at 5,000 μN for 4 hr and then loaded for four additional hours at 5,500 μN . Pillars 8–10 were loaded for 4 hr at 5,000 μN . The sliver of material attached to Pillar 10 is dust and not a result of the testing. Scale bar = 1 μm .

these bands or within the remainder of the pillars. Rather, the shear bands are characterized by zones of amorphous structure and small changes in crystallographic orientation. Figure 4a shows a high-angle annular dark field (HAADF) image of Pillar 10, with a shear band highlighted. This particular shear band is not oriented parallel to any low-index crystallographic plane. Figure 4b shows a high-resolution HAADF image of the shear band, which spans from the top-right corner to the bottom left, and has been highlighted as Region II. Lattice fringes are visible on either side of the shear band. We have denoted the upper-left and lower-right corners as Regions I and III, respectively, both of which are oriented approximately parallel to (010) with some out-of-plane tilt. We find the lattice on either side of the shear band has different orientations, as shown in the fast Fourier transform patterns (Wenk & Raymond, 1973) of Regions I–III in Figure 4c. We find an in-plane misorientation (rotation about [010]) of 5.4° between Regions I and III. From the lack of distinct diffraction spots in the fast Fourier transform pattern of Region II in Figure 4c, it is clear that the shear band is amorphous. Similar interruptions in the crystalline order were not observed away from the shear bands or in untested pillars.

We simultaneously acquired EEL spectrum images around the shear band to determine changes in the distribution of iron and magnesium with nanometer resolution. Figure 5a shows an HAADF image of a shear band in Pillar 10 with the region selected for EELS acquisition highlighted with a black square. Figure 5b shows the HAADF image of the shear band from the selected region that was acquired simultaneously during the EELS data set acquisition. Figures 5c and 5d show the relative composition maps of Fe and Mg, respectively. We find a higher concentration of Fe relative to Mg in the shear bands, in contrast to the rest of the sample. For instance, away from the shear band (Region I, Figure 5b), the relative abundance of Fe and Mg are $\sim 7\%$ and $\sim 93\%$, respectively, which is close to the composition determined by electron probe

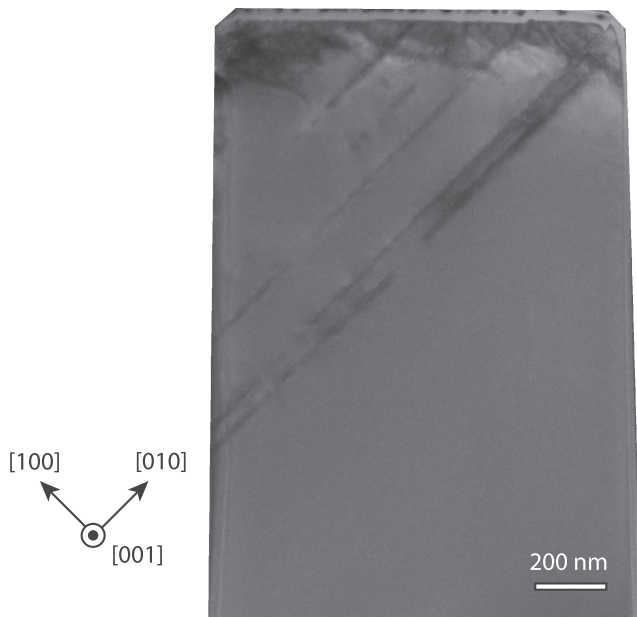


Figure 3. Bright field TEM image showing shear bands aligned with shear offsets on the surface of Pillar 7. The orientation of axial compression is vertical. In this pillar, shear bands are aligned in the (100) plane.

microanalysis (see section 2.1). In contrast, within the shear band (Region II, Figure 5b), the relative abundance of Fe and Mg are $\sim 14\%$ and $\sim 86\%$, respectively. In addition to the chemical segregation of Fe toward the shear band, we also observe changes in its oxidation state. Figure 5e shows the O K edge obtained from within the shear band (red line) and away from the shear band (green line), which are marked with red and green crosses in Figure 5b. We observe a prepeak at ~ 533 eV in the O K edge obtained from within the shear band, which is absent in the region away from it. The prepeak in the O K edge is attributed to electronic transitions from O 1s core states to unoccupied O 2p states that are hybridized to the empty states of neighboring atoms, specifically to the transition metal atoms (Luo et al., 2009; Mishra et al., 2016; Varela et al., 2009). A higher O K edge prepeak indicates a larger number of unoccupied O 2p states hybridized to Fe 3d states, which suggests a higher oxidation state of +3 for Fe. Similar changes in the O K edge spectra have been observed previously in olivine phases of Li_xFePO_4 ($x = 0, 0.6, 1$) (Miao et al., 2007; Nagpure et al., 2011), where Fe and O contribute toward charge compensation upon delithiation. We have used the O K edges in Figure 5e as reference spectra and performed a multiple linear least squares fitting of the entire EEL spectrum image data set to map the distribution of Fe^{2+} and Fe^{3+} , which are shown in Figure 5f. Besides the enrichment of Fe compared to Mg within the shear band, we also find Fe to be in the +3 oxidation state within the shear band, while away from the shear band, it is in the +2 oxidation state.

A similar examination was conducted on Pillar 6, which exhibited a sudden increase in displacement after 3,567 s at 5,500 μN . While this “catastrophic” failure is assumed to have produced the large shear offset observed in SEM (Figure 2), the pillar remained effectively intact. Notably, there was no evidence of voids or cracking along the shear plane observed during the FIB sectioning process. However, both changes in crystal orientation and amorphous regions were observed near the shear band, and EELS observations again indicate that Fe was in a +3 oxidation state near the band.

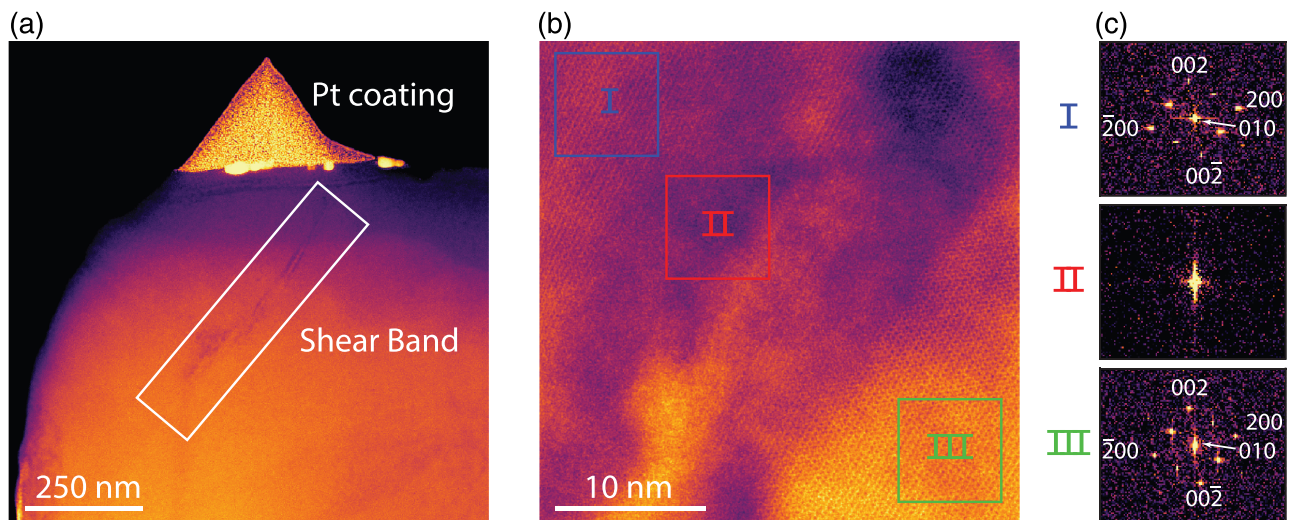


Figure 4. (a) Low-resolution HAADF image showing a shear band (white box) in Pillar 10. (b) High-resolution HAADF image around the shear band. (c) FFT patterns indicating the crystallographic orientations of Regions I–III highlighted in (b). Region II, which is inferred to be in the center of the shear band, is amorphous. In contrast, Regions I and III from the opposing sides of the shear band exhibit fully crystalline structure with no dislocations and are slightly misoriented.

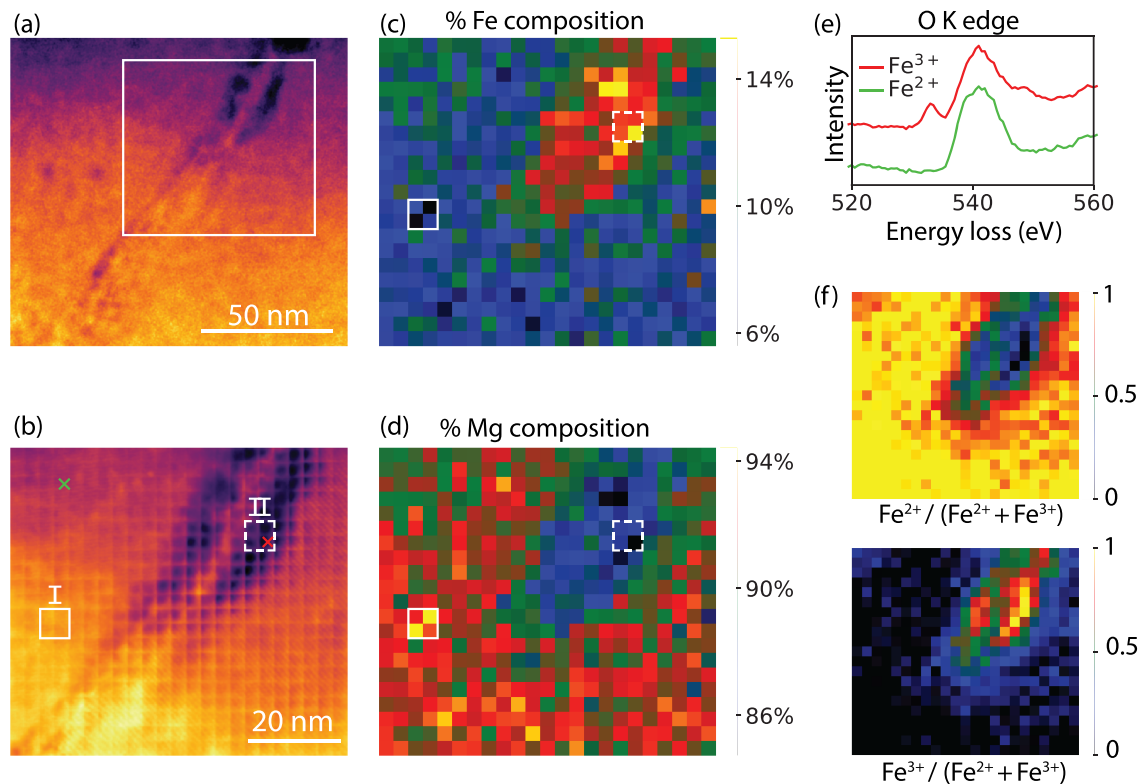


Figure 5. (a) HAADF image showing the region (white box) selected for EELS data acquisition in Pillar 10. (b) Simultaneously acquired HAADF image during EELS acquisition, with a 16×16 subpixel scanning enabled. EELS analysis resulted in the relative percentage composition maps of (c) Fe and (d) Mg, with their respective composition scales. (e) Spectra showing O K edge fine structure corresponding to Fe^{2+} (green) and Fe^{3+} (red), obtained from the corresponding beam positions identified with x-shaped symbols in (b). (f) Composition maps showing fraction of Fe^{2+} (top) and Fe^{3+} (bottom) with respect to the total Fe content. Shear bands are enriched in Fe and depleted in Mg, and the Fe in shear bands is largely in its 3+ state.

4. Discussion

As shown in Figure 1, catastrophic pillar failure took the form of axial splitting, mushrooming, or shear fracturing, all of which have been observed as failure modes in monotonic testing of brittle materials (Howie et al., 2012). The distribution of dwell times observed before failure indicates that the deformation process continues throughout the creep test until a criticality is reached that most often causes complete or nearly complete failure along a fracture surface. This behavior is reminiscent of fracture caused by the nucleation, growth, and coalescence of microcracks (Hsueh & Evans, 1981; Lockner et al., 1991). It is conceivable in this case that deformation occurs along a favorable orientation but is then obstructed by an obstacle with a large energy barrier, causing a buildup of stress behind the obstacle that ultimately results in cleavage failure along the slip plane (Ashby & Verrall, 1977).

The fact that room temperature plasticity was observed at all in olivine in the present work is in itself remarkable, as this has not been reported previously using traditional testing methods at larger scales. Also surprisingly, no evidence of dislocation slip was observed in the deformed micropillars; STEM results suggest instead that the plastic deformation is associated with the formation and/or propagation of amorphous shear bands oriented at $\sim 45^\circ$ to the loading direction. It is difficult to form glasses from natural olivine ($\text{Mg}_{2-x}\text{Fe}_x\text{SiO}_4$) and the related end-member structures of forsterite (Mg_2SiO_4) and fayalite (Fe_2SiO_4) due to the isolated nature of SiO_4^{4-} tetrahedra in the structure. However, these materials have been shown to undergo amorphization under high-pressure and shock-loading conditions (Andrault et al., 1995; Guyot & Reynard, 1992; Jeanloz, 1980; Jeanloz et al., 1977; Richard & Richet, 1990; Santamaria-Perez et al., 2016; Williams et al., 1990). These prior observations were made during or after loading of bulk specimens to several tens of gigapascal, much higher than the uniaxial compression stress applied to the micropillars in the present work (~ 4 GPa). Interestingly, recent first-principle calculations

Table 2

Properties of the Pillars Shown in Figure 2, Including Their Measured Strain Rate and Maximum Applied Stress From Table 1

Pillar #	Measured strain rate (s^{-1})	Maximum applied stress (GPa)	Stress (GPa)				
			$p = 1/2 \ q = 1$	$p = 3/4 \ q = 4/3$	$p = 1 \ q = 2$	$p = 2/3 \ q = 2$	$p = 1 \ q = 1$
7	4×10^{-6}	4.4	3.91	3.93	3.9	3.53	4.19
Percent difference:			11.4%	10.9%	11.6%	20.0%	5.0%
8	1×10^{-6}	4.1	3.82	3.85	3.82	3.41	4.14
Percent difference:			7.7%	7.0%	7.7%	17.6%	0.0%
10	5×10^{-7}	4.1	3.76	3.81	3.78	3.76	4.10
Percent difference:			9.2%	8.0%	8.7%	9.2%	1.0%

Note: The maximum applied stress is compared with the flow stress given by five different low-temperature plasticity flow laws (Equation 6) at the corresponding strain rate. The difference between the maximum applied stress and the stress from the flow law, relative to the applied stress, is also provided.

suggest that the ideal shear strength of olivine single crystals is anisotropic and of a similar magnitude to the stresses imposed during micropillar compression testing, ranging from 5.6–11.5 GPa (Gouriet et al., 2019). The mechanism by which the misorientation and amorphization develop at low stresses in micropillar compression experiments is unclear, although it is likely the result of a Mode III-type shear process severely distorting the lattice and disrupting the local bonding and crystalline structure. In their work on pressure-induced amorphization in olivine with varying Mg : Fe ratios, Andraut et al. (1995) noted that compression anisotropy increases as the Fe content increases and suggested that the maximum distortion that olivine can withstand prior to amorphization is therefore lower in Fe-rich compositions. In the present work, we note that the amorphous regions identified postdeformation are enriched in Fe at the expense of Mg. Although the deformation was time dependent, diffusive redistribution of the Mg and Fe over length scales of tens of nanometer is not expected at the relatively low homologous temperature and short durations over which the experiments were performed. Moreover, we also observed nanoscale variations in the distribution of Fe and Mg in undeformed olivine and postulate that the observed deformation bands may initiate preferentially in regions with preexisting Fe enrichment. In addition to being more prone to amorphization, these compositional inhomogeneities also may act as stress concentrators in the structure, increasing the driving force to activate the Mode III misorientation process. These misoriented regions may then generate dislocations or form cracks during deformation of bulk specimens.

The amorphous bands also exhibit an increase in the oxidation state of Fe from 2+ to 3+. In the absence of an oxidizing environment, this change in state suggests the creation of cation vacancies or oxygen interstitials in the structure—even at the low homologous temperature of the experiments. These observations of atomic migration of Mg/Fe and increase in oxidation state of iron can be explained with first-principle calculations of the formation energy of Mg vacancies and their migration barriers in isomorphous forsterite (Mg_2SiO_4). Using density functional theory, Verma and Karki (2009) report that formation energy of Mg vacancies is low; hence, they are expected to exist in larger concentrations compared to Si vacancies. They also report that the migration barrier for Mg^{2+} ions to hop into a neighboring Mg vacancy site is relatively small (0.77 eV at 0 GPa), which is in good agreement with an experimentally observed value of 0.64 eV in iron-containing forsterite (Jaoul et al., 1995).

The observed room temperature creep deformation occurred during sustained loading at uniaxial stresses that fell from initial values of 4.1–4.4 to 3.7–4.0 GPa after 4 hr. These measurements are in excellent agreement with the low-temperature plasticity flow law fits determined in a previous nanoindentation study (Kranjc et al., 2016). The uniaxial creep strain rates measured indirectly through stiffness changes observed during the superimposed cyclic loading were on the order of 10^{-6} to $10^{-7} s^{-1}$. (It was not possible to verify the total displacements associated with those strain rates and predicted from equation 2c because the displacements were on the order of the error of the height measurements obtained through the SEM image analysis.) In Table 2, the calculated strain rates and maximum stress applied to the micropillars in Table 1 are compared to stresses given by the low-temperature plasticity flow law obtained from nanoindentation testing in Kranjc et al. (2016):

$$\dot{\epsilon}_{LTP} = A\sigma^2 \exp\left\{-\left(\frac{H_0^*}{RT}\right)\left(1-\left(\frac{\sigma}{\sigma_p}\right)^p\right)^q\right\}, \quad (6)$$

where $\dot{\epsilon}_{LTP}$ is the strain rate, H_0^* is the zero-stress activation enthalpy, σ_p is the Peierls stress, and A is a material-dependent parameter. Dimensionless constants p and q depend on the details of the deformation mechanism and are constrained to fall within ranges $0 \leq p \leq 1$ and $1 \leq q \leq 2$ (Kocks et al., 1975). The measured strain rate and testing temperature (ambient) were inserted into equation 6, with the same constants as calculated in Kranjc et al. (2016) for the five different flow laws obtained through our nanoindentation testing. The difference between the flow laws and the pillar measurements varied from as high as 20% to as low as 0%. The flow law that consistently gave the smallest error was that with $p = 1$ and $q = 1$.

It is important to note here that size can affect the compressive yield strength of crystalline materials, with nanoscale specimens exhibiting yield strengths over an order of magnitude greater than their bulk counterparts (Greer & Nix, 2006). This behavior is often attributed to fewer dislocation sources (Oh et al., 2009) and “dislocation starvation,” where dislocations are annihilated at the sample surfaces instead of interacting within the sample volume (Greer & Nix, 2006). However, this yield strength effect is much more pronounced in metallic materials than in ceramics, where the yield strength is closer to the theoretical strength and the dislocation activation volume is smaller (Korte et al., 2011; Korte & Clegg, 2011). This size effect on strength is most likely not a concern here since the material is ceramic, and no dislocation activity is observed in the STEM images of the deformed specimens. Furthermore, there is good agreement between the predicted flow law and the measured values, without any correction based on size (Kumamoto et al., 2017). Overall, the fact that there is agreement from the data obtained using two different methods, micropillar compression and nanoindentation, suggests that these complementary approaches will allow continued refinement of viscoplastic flow laws at low homologous temperatures.

5. Conclusions

Room temperature creep deformation was achieved in tests conducted on 1.25- μm diameter pillars fabricated from a [110]_c oriented single crystal of olivine. Deformation occurred at sustained compressive stresses of approximately 4 GPa, in excellent agreement with low-temperature plasticity flow law fits determined in an earlier nanoindentation study (Kranjc et al., 2016). The majority of the micropillars deformed by brittle mechanisms or catastrophic shear failure after dwell times ranging from several seconds to several hours. However several pillars exhibit evidence for stable plastic distortion. Surprisingly, there was no evidence of dislocation activity in the deformed pillars. Instead, the creep deformation was associated with the formation and/or propagation of amorphous bands separating regions where the crystal was misoriented. The amorphous regions were found to be enriched in Fe relative to Mg, with most of the Fe being in +3 oxidation state within the shear band compared to their +2 state in the bulk. The low calculated formation energy of Mg vacancies combined with low migration barrier for Mg hopping may help to explain the creep deformation and associated diffusional segregation observed using STEM-EELS. We also observe nanoscale variations in the cation distribution in undeformed olivine samples that may promote the observed amorphization and creep diffusion. These studies are ongoing and will be reported elsewhere. Although the mechanisms of deformation during micropillar compression and nanoindentation may be different, the measured or calculated yield strengths are largely similar. This suggests that the stresses required to induce dislocation glide during nanoindentation experiments may be closely related to the stresses required to fully amorphize the olivine lattice. Further experiments and calculations are needed to evaluate this hypothesis.

References

- Andraut, D., Bouhifd, M. A., Itie, J. P., & Richet, P. (1995). Compression and amorphization of (Mg,Fe)₂SiO₄ olivines: An X-ray diffraction study up to 70 GPa. *Physics and Chemistry of Minerals*, 22, 99–107.
- Ashby, M. F., & Verrall, R. A. (1977). Micromechanisms of flow and fracture, and their relevance to the rheology of the upper mantle. *Philosophical Transactions of Royal Society London A*, 288, 59–95.
- Bai, Q., & Kohlstedt, D. L. (1992). High-temperature creep of olivine single crystals, 2. Dislocation structures. *Tectonophysics*, 206(1–2), 1–29.
- Banerjee, A., Bernoulli, D., Zhang, H., Yuen, M. F., Liu, J., Dong, J., et al. (2018). Ultralarge elastic deformation of nanoscale diamond. *Science*, 360(6386), 300–302. <https://doi.org/10.1126/science.aar4165>

Acknowledgments

The sample tested here is identified in the manuscript (Table 11) using the IGSN registration number provided by SESAR. Additional data are archived using the Open Scholarship Data Repository (doi:10.7936/dwtx-rc52). This work was supported by the National Science Foundation under Grant No. EAR-17-26165. The authors also acknowledge financial support from Washington University in St. Louis and the Institute of Materials Science and Engineering (IMSE) for the use of the SEM and TEM and for staff assistance. TEM foils were prepared with financial support of the University of Michigan College of Engineering and technical support from the Michigan Center for Materials Characterization. STEM work performed at Oak Ridge National Laboratory was supported by the U.S. Department of Energy, Office of Science, Basic Energy Sciences Materials Science and Engineering Division (BES-MSED). The authors thank the Washington University Center for Cellular Imaging (WUCCI) for their assistance in fabricating the FIB micropillars, Paul Carpenter for his assistance with the EPMA, and Mike Sly for his contributions. Two anonymous reviewers are thanked for their constructive comments.

- Bharathula, A., Lee, S. W., Wright, W. J., & Flores, K. M. (2010). Compression testing of metallic glass at small length scales: Effects on deformation mode and stability. *Acta Materialia*, *58*(17), 5789–5796. <https://doi.org/10.1016/j.actamat.2010.06.054>
- Christensen, N. I. (1996). Poisson's ratio and crustal seismology. *Journal of Geophysical Research*, *101*(B2), 3139–3156. <https://doi.org/10.1029/95JB03446>
- Druiventak, A., Trepman, C. A., Renner, J., & Hanke, K. (2011). Low-temperature plasticity of olivine during high stress deformation of peridotite at lithospheric conditions—An experimental study. *Earth and Planetary Science Letters*, *311*, 199–211.
- Durham, W. B., & Goetze, C. (1977). Plastic flow of oriented single crystals of olivine. *Journal of Geophysical Research*, *82*(36), 5737–5753.
- Evans, B., & Goetze, C. (1979). The temperature variation of hardness of olivine and its implication for polycrystalline yield stress. *Journal of Geophysical Research*, *84*(B10), 5505–5524. <https://doi.org/10.1029/JB084iB10p05505>
- Freed, A. M., Bürgmann, R., Calais, E., Freymueller, J., & Hreinsdóttir, S. (2006). Implications of deformation following the 2002 Denali, Alaska, earthquake for postseismic relaxation processes and lithospheric rheology. *Journal of Geophysical Research*, *111*, B01401. <https://doi.org/10.1029/2005JB003894>
- Gao, H., Ji, B., Jager, I. L., Arzt, E., & Fratzl, P. (2003). Materials become insensitive to flaws at nanoscale: Lessons from nature. *Proceedings of the National Academy of Sciences*, *100*(10), 5597–5600. <https://doi.org/10.1073/pnas.0631609100>
- Gouriet, K., Carrez, P., & Cordier, P. (2019). Ultimate mechanical properties of Forsterite. *Minerals*, *9*(12), 787.
- Greer, J. R., & Nix, W. D. (2006). Nanoscale gold pillars strengthened through dislocation starvation. *Physical Review B: Condensed Matter and Materials Physics*, *73*(24), 1–6. <https://doi.org/10.1103/PhysRevB.73.245140>
- Guyot, F., & Reynard, B. (1992). Pressure-induced structural modifications and amorphization in olivine compounds. *Chemical Geology*, *96*(3–4), 411–420. [https://doi.org/10.1016/0009-2541\(92\)90069-H](https://doi.org/10.1016/0009-2541(92)90069-H)
- Hansen, L. N., Zimmerman, M. E., & Kohlstedt, D. L. (2011). Grain boundary sliding in San Carlos olivine: Flow law parameters and crystallographic-preferred orientation. *Journal of Geophysical Research*, *116*, B08201. <https://doi.org/10.1029/2011JB008220>
- Hirth, G., & Kohlstedt, D. L. (2003). Rheology of the upper mantle and the mantle wedge: A view from the experimentalists. *Inside the Subduction Factory*, *138*, 83–105.
- Hirth, G., & Kohlstedt, D. L. (2015). The stress dependence of olivine creep rate: Implications for extrapolation of lab data and interpretation of recrystallized grain size. *Earth and Planetary Science Letters*, *418*, 20–26.
- Howie, P. R., Korte, S., & Clegg, W. J. (2012). Fracture modes in micropillar compression of brittle crystals. *Journal of Materials Research*, *27*(1), 141–151. <https://doi.org/10.1557/jmr.2011.256>
- Hsueh, C. H., & Evans, A. G. (1981). Creep fracture in ceramic polycrystals-II. Effects of inhomogeneity on creep rupture. *Acta Metallurgica*, *29*(12), 1907–1917. [https://doi.org/10.1016/0001-6160\(81\)90028-6](https://doi.org/10.1016/0001-6160(81)90028-6)
- Hütsch, J., & Lilleodden, E. T. (2014). The influence of focused-ion beam preparation technique on microcompression investigations: Lathe vs. annular milling. *Scripta Materialia*, *77*, 49–51. <https://doi.org/10.1016/j.scriptamat.2014.01.016>
- Jain, C., Korenaga, J., & Karato, S. I. (2017). On the yield strength of oceanic lithosphere. *Geophysical Research Letters*, *44*, 9716–9722. <https://doi.org/10.1002/2017GL075043>
- Jang, D., & Greer, J. R. (2010). Transition from a strong-yet-brittle to a stronger-and-ductile state by size reduction of metallic glasses. *Nature Materials*, *9*(3), 215–219. <https://doi.org/10.1038/nmat2622>
- Jaoul, Ö., Bertran-Alvarez, Y., Liebermann, R. C., & Price, G. D. (1995). Fe–Mg interdiffusion in olivine up to 9 GPa at T=600–900 °C; Experimental data and comparison with defect calculations. *Physics of the Earth and Planetary Interiors*, *89*(3–4), 199–218.
- Jaroslów, G. E., Hirth, G., & Dick, H. J. B. (1996). Abyssal peridotite mylonites: Implications for grain-size sensitive flow and strain localization in the oceanic lithosphere. *Tectonophysics*, *256*, 17–37.
- Jeanloz, R. (1980). Shock effects in olivine and implications for Hugoniot data. *Journal of Geophysical Research*, *85*(B6), 3163–3176.
- Jeanloz, R., Ahrens, T. J., Lally, J. S., Nord, G. L. Jr., Christieand, J. M., & Heuer, A. H. (1977). Shock-produced olivine glass: First observation. *Science*, *197*(4302), 457–459. <https://doi.org/10.1126/science.197.4302.457>
- Karato, S. I., & Wu, P. (1993). Rheology of the upper mantle: A synthesis. *Science*, *260*(5109), 771–778. <https://doi.org/10.1126/science.260.5109.771>
- Kocks, U. F., Argon, A. S., & Ashby, M. F. (1975). *Thermodynamics and kinetics of slip*. Oxford, U. K.: Pergamon Press.
- Korte, S., Barnard, J. S., Stearn, R. J., & Clegg, W. J. (2011). Deformation of silicon-Insights from microcompression testing at 25–500 C. *International Journal of Plasticity*, *27*(11), 1853–1866. <https://doi.org/10.1016/j.ijplas.2011.05.009>
- Korte, S., & Clegg, W. J. (2009). Micropillar compression of ceramics at elevated temperatures. *Scripta Materialia*, *60*(9), 807–810. <https://doi.org/10.1016/j.scriptamat.2009.01.029>
- Korte, S., & Clegg, W. J. (2011). Discussion of the dependence of the effect of size on the yield stress in hard materials studied by microcompression of MgO. *Philosophical Magazine*, *91*(7–9), 1150–1162. <https://doi.org/10.1080/14786435.2010.505179>
- Kranjc, K., Rouse, Z., Flores, K. M., & Skemer, P. (2016). Low-temperature plastic rheology of olivine determined by nanoindentation. *Geophysical Research Letters*, *43*, 176–184. <https://doi.org/10.1002/2015GL065837>
- Kumamoto, K. M., Thom, C. A., Wallis, D., Hansen, L. N., Armstrong, D. E. J., Warren, J. M., et al. (2017). Size effects resolve discrepancies in 40 years of work on low-temperature plasticity in olivine. *Science Advances*, *3*(9), e1701338. <https://doi.org/10.1126/sciadv.1701338>
- Lockner, D. A., Byerlee, J. D., Kuksenko, V., Ponomarev, A., & Sidorin, A. (1991). Quasi-static fault growth and shear fracture energy in granite. *Nature*, *350*(6313), 39–42.
- Luo, W., Varela, M., Tao, J., Pennycook, S. J., & Pantelides, S. T. (2009). Electronic and crystal-field effects in the fine structure of electron energy-loss spectra of manganites. *Physical Review B*, *79*(5), 052405. <https://doi.org/10.1103/PhysRevB.79.052405>
- Mei, S., & Kohlstedt, D. L. (2000a). Influence of water on plastic deformation of olivine aggregates 1: Diffusion creep regime. *Journal of Geophysical Research*, *105*, 21,457–21,469.
- Mei, S., & Kohlstedt, D. L. (2000b). Influence of water on plastic deformation of olivine aggregates 2. Dislocation creep regime. *Journal of Geophysical Research*, *105*, 21,471–21,481.
- Mei, S., Suzuki, A. M., Kohlstedt, D. L., Dixon, N. A., & Durham, W. B. (2010). Experimental constraints on the strength of the lithospheric mantle. *Journal of Geophysical Research*, *115*, B8204. <https://doi.org/10.1029/2009JB006873>
- Miao, S., Kicher, M., Rez, P., Fultz, B., Yazami, R., & Ahn, C. C. (2007). Local electronic structure of olivine phases of Li_xFePO₄. *The Journal of Physical Chemistry. A*, *111*(20), 4242–4247.
- Mishra, R., Kim, Y.-M., He, Q., Huang, X., Kim, S. K., Susner, M. A., et al. (2016). Towards spin-polarized two-dimensional electron gas at a surface of an antiferromagnetic insulating oxide. *Physical Review B*, *94*(4), 045123.
- Nagpure, S. C., Babu, S. S., Bhushan, B., Kumar, A., Mishra, R., Windl, W., et al. (2011). Local electronic structure of LiFePO₄ nanoparticles in aged Li-ion batteries. *Acta Materialia*, *59*(18), 6917–6926.

- Nicolas, A., Bouchez, J. L., Boudier, F., & Mercier, J. C. (1971). Textures, structures and fabrics due to solid state flow in some European lherzolites. *Tectonophysics*, *12*(1), 55–86.
- Oh, S. H., Legros, M., Kiener, D., & Dehm, G. (2009). In situ observation of dislocation nucleation and escape in a submicrometre aluminium single crystal. *Nature Materials*, *8*(2), 95–100. <https://doi.org/10.1038/nmat2370>
- Östlund, F., Howie, P. R., Ghisleni, R., Korte, S., Leifer, K., Clegg, W. J., & Michler, J. (2011). Ductile–brittle transition in micropillar compression of GaAs at room temperature. *Philosophical Magazine*, *91*(7–9), 1190–1199. <https://doi.org/10.1080/14786435.2010.509286>
- Östlund, F., Rzepiejewska-Malyska, K., Leifer, K., Hale, L. M., Tang, Y., Ballarini, R., et al. (2009). Brittle-to-ductile transition in uniaxial compression of silicon pillars at room temperature. *Advanced Functional Materials*, *19*(15), 2439–2444. <https://doi.org/10.1002/adfm.200900418>
- Raterron, P., Wu, Y., Weidner, D. J., & Chen, J. (2004). Low-temperature olivine rheology at high pressure. *Physics of the Earth and Planetary Interiors*, *145*(1), 149–159.
- Richard, G., & Richet, P. (1990). Room-temperature amorphization of fayalite and high-pressure properties of Fe₂SiO₄ liquid. *Geophysical Research Letters*, *17*(12), 2093–2096.
- Santamaria-Perez, D., Thomson, A., Segura, A., Pellicer-Torres, J., Manjon, F. J., Corà, F., et al. (2016). Metastable structural transformations and pressure-induced amorphization in natural (Mg,Fe)₂SiO₄ olivine under static compression: A Raman spectroscopic study. *American Mineralogist*, *101*, 1642–1650.
- Sneddon, I. (1965). The relation between load and penetration in the axisymmetric Boussinesq problem for a punch of arbitrary profile. *International Journal of Engineering Science*, *3*(1), 47–57.
- Varela, M., Oxley, M. P., Luo, W., Tao, J., Watanabe, M., Lupini, A. R., et al. (2009). Atomic-resolution imaging of oxidation states in manganites. *Physical Review B*, *79*(8), 085117.
- Verma, A. K., & Karki, B. B. (2009). Ab initio investigations of native and protonic point defects in Mg₂SiO₄ polymorphs under high pressure. *Earth and Planetary Science Letters*, *285*(1–2), 140–149.
- Volkert, C. A., Donohue, A., & Spaepen, F. (2008). Effect of sample size on deformation in amorphous metals. *Journal of Applied Physics*, *103*, 83539. <https://doi.org/10.1063/1.2884584>
- Wenk, H. R., & Raymond, K. N. (1973). Four new structure refinements of olivine. *Zeitschrift für Kristallographie-Crystalline Materials*, *137*(1), 86–105.
- Williams, Q., Knittle, E., Reichlin, R., Martin, S., & Jeanloz, R. (1990). Structural and electronic properties of Fe₂SiO₄-fayalite at ultrahigh pressures' amorphization and gap closure. *Journal of Geophysical Research*, *95*(B13), 21,549–21,563.